

In situ formed partially disordered phases as earth-abundant Mn-rich cathode materials

Received: 3 March 2023

Accepted: 6 September 2023

Published online: 5 October 2023

Check for updates

Zijian Cai^{1,2,11}, Bin Ouyang^{3,11}, Han-Ming Hau^{1,2}, Tina Chen^{1,2},
Raynald Giovine^{4,5}, Krishna Prasad Koirala⁶, Linze Li⁷, Huiwen Ji⁸, Yang Ha⁹,
Yingzhi Sun^{1,2}, Jianping Huang², Yu Chen^{1,2}, Vincent Wu^{4,5}, Wanli Yang⁹,
Chongmin Wang⁷, Raphaële J. Clément^{4,5}, Zhengyan Lun^{1,2,10} ✉ &
Gerbrand Ceder^{1,2} ✉

Earth-abundant cathode materials are urgently needed to enable scaling of the Li-ion industry to multiply terawatt hours of annual production, necessitating reconsideration of how good cathode materials can be obtained. Irreversible transition metal migration and phase transformations in Li-ion cathodes are typically believed to be detrimental because they may trigger voltage hysteresis, poor kinetics and capacity degradation. Here we challenge this conventional consensus by reporting an unusual phase transformation from disordered Li- and Mn-rich rock salts to a new phase (named δ), which displays partial spinel-like ordering with short coherence length and exhibits high energy density and rate capability. Unlike other Mn-based cathodes, the δ phase exhibits almost no voltage fade upon cycling. We identify the driving force and kinetics of this in situ cathode formation and establish design guidelines for Li- and Mn-rich compositions that combine high energy density, high rate capability and good cyclability, thereby enabling Mn-based energy storage.

As the prime energy storage technology, Li-ion batteries have experienced a rapid growth in demand, which strains supplies of minerals necessary for the technology, with nickel and cobalt being of particular concern. By 2035, the annual production of Li-ion batteries is expected to reach multiple terawatt hours (TWh), requiring several million tons of redox-active transition metals (TMs) to produce cathode materials. The only TMs produced in large enough quantities to satisfy this demand without a notable price increase are Ti, Cr, Mn, Fe and Cu. The low voltage of Ti and Cu prevents their use as cathode active redox couples. The Fe²⁺/Fe³⁺ redox couple has too low a voltage in close-packed oxides to achieve reasonable energy density, though it can be raised in polyanion

materials such as LiFePO₄ at the expense of energy density. While Cr is a very attractive redox couple, the toxicity of Cr⁶⁺ has led to hesitation in its use for Li-ion batteries. This leaves Mn as the most viable redox couple for inexpensive and earth-abundant Li-intercalation cathodes. Indeed, LiMn₂O₄ spinels were used in early batteries for electric vehicles (EVs) but suffered from rather low energy density and stability problems^{1–4}. In today's EV batteries, Mn is used as an inactive element in the Li(Ni,Mn,Co)O₂ (NMC)-type cathodes, though in Li-rich NMCs, its redox can be partially activated upon oxygen loss in the first few cycles^{5–13}.

The challenge with Mn-based intercalation cathodes is the relative mobility of both the Mn²⁺ and Mn³⁺ ion (through disproportionation)

¹Department of Materials Science and Engineering, University of California Berkeley, Berkeley, CA, USA. ²Materials Sciences Division, Lawrence Berkeley National Laboratory, Berkeley, CA, USA. ³Department of Chemistry and Biochemistry, Florida State University, Tallahassee, FL, USA. ⁴Materials Department, University of California Santa Barbara, Santa Barbara, CA, USA. ⁵Materials Research Laboratory, University of California Santa Barbara, Santa Barbara, CA, USA. ⁶Physical and Computational Sciences Directorate, Pacific Northwest National Laboratory, Richland, WA, USA. ⁷Environmental Molecular Sciences Laboratory, Pacific Northwest National Laboratory, Richland, WA, USA. ⁸Department of Materials Science and Engineering, University of Utah, Salt Lake City, UT, USA. ⁹The Advanced Light Source, Lawrence Berkeley National Laboratory, Berkeley, CA, USA. ¹⁰School of Chemical Sciences, University of Chinese Academy of Sciences, Beijing, China. ¹¹These authors contributed equally: Zijian Cai, Bin Ouyang. ✉e-mail: zylun@ucas.ac.cn; gceder@berkeley.edu

in a closed-packed oxygen lattice, making the design of well-ordered compounds challenging as they rapidly transform during cycling. Indeed, both layered LiMnO_2 and orthorhombic LiMnO_2 transform to a spinel structure within just a few charge/discharge cycles^{14–20}. Some Li-excess disordered rock salts (DRX) were also reported to transform towards spinel order upon cycling^{21–23}. Spinel LiMn_2O_4 is the only ordered Mn compound that does not undergo structural changes upon cycling, but its theoretical capacity of 296 mAh g^{-1} is not practically accessible because of the detrimental collective two-phase reaction at -3 V (ref. 1). More recently, partially (dis)ordered Li–Mn–O–F spinels with cation over-stoichiometry (Fig. 1a) have demonstrated ultrahigh energy and power density by removing the two-phase region^{24,25}. In a perfectly ordered spinel LiMn_2O_4 , Li and Mn occupy the $8a$ tetrahedral and $16d$ octahedral sites, respectively. Synthesis through ball milling can create $16c/16d$ disorder with partial occupancy of the otherwise empty $16c$ site, which has been shown to be essential to transform the 3 V two-phase region between LiMn_2O_4 and $\text{Li}_2\text{Mn}_2\text{O}_4$ into a solid solution²⁶ and thereby enhance the capacity, rate capability and stability of the spinel. While this work has demonstrated an opportunity for creating a high-capacity Mn-based material, ball milling synthesis is not suitable to produce cathode materials at scale.

In this Article, we implement a strategy that incorporates the high mobility of Mn and the intrinsic stability of the spinel-like ordering to create high energy density earth-abundant cathode materials. Our approach is to start from a high-Mn-content DRX and let it transform by electrochemical cycling into a partially disordered spinel-like phase with short coherence length (termed the δ phase). Immobile Ti^{4+} ions are added to prevent the formation of complete and long-range spinel order thereby retaining solid-solution behaviour over the large capacity range. Unlike Li-rich, Mn-rich NMC cathodes (LMR-NMCs) and LiMnO_2 , which show voltage decay^{16–19}, the DRX to δ phase transformation produces no observable voltage fade because of the formation of the additional -4 V plateau-like feature, characteristic of spinel-type ordering. A high capacity (specific energy) of 288.6 mAh g^{-1} (826 Wh kg^{-1}) is reached after transformation, with only 83 mV voltage drop when cycled between 1.5 and 5 V for 100 cycles. Cycling in the narrower voltage window of 2 – 4.8 V leads to an average voltage increase of 37 mV after 100 cycles. The advantage of creating a partially disordered structure is not only applicable to DRX compounds but is also potentially applicable to LMR-NMCs.

We study the formation of the high-capacity δ -structure in $\text{Li}_{1+x}\text{Mn}_{1-3x}\text{Ti}_{2x}\text{O}_2$ ($x = 0.05, 0.1$ and 0.15), which contain only inexpensive Mn and Ti as TMs. We find that increasing the Mn content leads to more rapid formation of the δ phase upon cycling. Evaluating the kinetics of TM migration and the thermodynamic driving forces, we show that the formation of the δ phase is universal for Mn-rich DRX compounds. Finally, we propose various design strategies to enable the transformation to the δ phase and explain why its unique partial ordering leads to a high-capacity cathode material.

Electrochemistry of a series of Mn-based DRX compounds

We synthesized a series of DRX compounds with different Li excess and Mn content (but identical Mn valence) via a solid-state method. The Mn content is systematically decreased from $\text{Li}_{1.05}\text{Mn}_{0.85}\text{Ti}_{0.1}\text{O}_2$ (L5M85) to $\text{Li}_{1.10}\text{Mn}_{0.7}\text{Ti}_{0.2}\text{O}_2$ (L10M70) and further to $\text{Li}_{1.15}\text{Mn}_{0.55}\text{Ti}_{0.3}\text{O}_2$ (L15M55). The theoretical capacity based on Li content and $\text{Mn}^{3/4+}$ redox are calculated and shown in Supplementary Table 1. X-ray diffraction (XRD) patterns, presented in Fig. 1b, show that all three samples form a pure DRX phase with small amount of Li_2CO_3 impurity (5.5%, 5.6% and 4.0% for L5M85, L10M70 and L15M55, respectively; Supplementary Tables 2–4). Scanning transmission electron microscopy (STEM) and energy-dispersive X-ray spectroscopy (EDS) results on a representative L5M85 sample are presented in Fig. 1f and

confirm a homogeneous distribution of Mn, Ti and O. The diffraction spots in the selected area electron diffraction (SAED) pattern (Fig. 1g) can be indexed to the $Fm\bar{3}m$ space group of the rock salt lattice. The square-like diffuse scattering is the result of short-range cation order, as documented in other DRX compounds²⁷. The as-synthesized materials were shaker milled with carbon for electrode fabrication. Scanning electron microscopy (SEM) to characterize the particle morphology after the milling process is shown for L5M85 (Fig. 1c), L10M70 (Fig. 1d) and L15M55 (Fig. 1e) and confirms a primary particle size of 200 – 600 nm in all three samples.

The electrochemical performance of the three compounds was evaluated using galvanostatic cycling between 2 and 4.8 V at 20 mAh g^{-1} . As shown in Fig. 2a, the initial charge (discharge) capacity increases with the amount of Li excess from 220 mAh g^{-1} (138 mAh g^{-1}) for L5M85 to 270 mAh g^{-1} (156 mAh g^{-1}) for L10M70 and further to 314 mAh g^{-1} (206 mAh g^{-1}) for L15M55. Due to the lack of long-range cation order in DRX, Li-ion transport relies on the statistical percolation of low-barrier O-TM tetrahedra, where no TMs face share with the tetrahedral sites²⁸. A higher Li content generally leads to a better O-TM percolation network and, thus, to a higher capacity, which is consistent with the electrochemical performance of the three DRX compounds.

The voltage curves are similar for all three compounds in the initial cycle but become very different upon cycling, as shown in Fig. 2a, while the redox mechanism remains similar at the first and 20th cycle (Supplementary Notes 1 and 2). After 20 cycles, the dQ/dV curve (inset in Fig. 2a) shows that two plateau-like features can be observed in L5M85. These two additional features are weaker in L10M70 and are absent in L15M55. To compare the structural evolution that is responsible for these changes in the voltage profile, ex situ synchrotron XRD was performed on cathode films of L5M85, L10M70 and L15M55 discharged to 3.5 V at the 20th cycle, as shown in Fig. 2b. In addition to the rock salt peaks, L5M85 shows broad, yet strong additional peaks marked by asterisks in Fig. 2b. These peaks indicate the formation of a lower symmetry environment. With increasing Li content (decreasing Mn content) from L5M85 to L15M55, the additional diffraction peaks become weaker. Detailed structural characterization of the structure formed upon cycling will be presented in the next section, but based on the voltage profiles and XRD patterns, it is clear that a low Li excess level and high-Mn content promote the structural change from DRX to a new phase with lower symmetry.

The capacity evolution (Fig. 2c) of the compounds upon cycling is closely linked to their structural change. For L5M85, the discharge capacity increases by more than 50% over the first 20 cycles (from 138 mAh g^{-1} to 211 mAh g^{-1}). L10M70 also experiences a capacity increase but at a much slower rate, with the maximum capacity of 202 mAh g^{-1} obtained at the 44th cycle. In contrast, L15M55 shows continuous capacity decay from the first cycle. We note that although the structural change leads to an increase in capacity, other factors, such as electrolyte decomposition or Mn dissolution (Supplementary Fig. 1), could degrade performance, and the overall capacity evolution upon cycling is a complex competition between these factors.

L5M85 exhibits excellent voltage retention despite the structural change that occurs upon cycling, as shown in Fig. 2d, in sharp contrast with many previously reported Mn-rich cathodes^{29–31}. The average discharge voltage increases from 3.128 V to 3.191 V during the first 40 cycles when cycled between 2 and 4.8 V (Fig. 2d). After 100 cycles, L5M85 still retains a discharge voltage of 3.165 V , which is 37 mV higher than its initial value and only 26 mV lower than its maximum value at cycle 41. Even when cycled over a very wide voltage window, 1.5 – 5 V , the average voltage decreases from its maximum of 2.889 V to 2.806 V at the 100th cycle, with a decay of only 83 mV . These small voltage changes are not necessarily related to the material but may reflect a polarization increase due to electrolyte breakdown, which has been well documented for DRX compounds cycling to high voltage^{32,33}. The polarization growth is evidenced

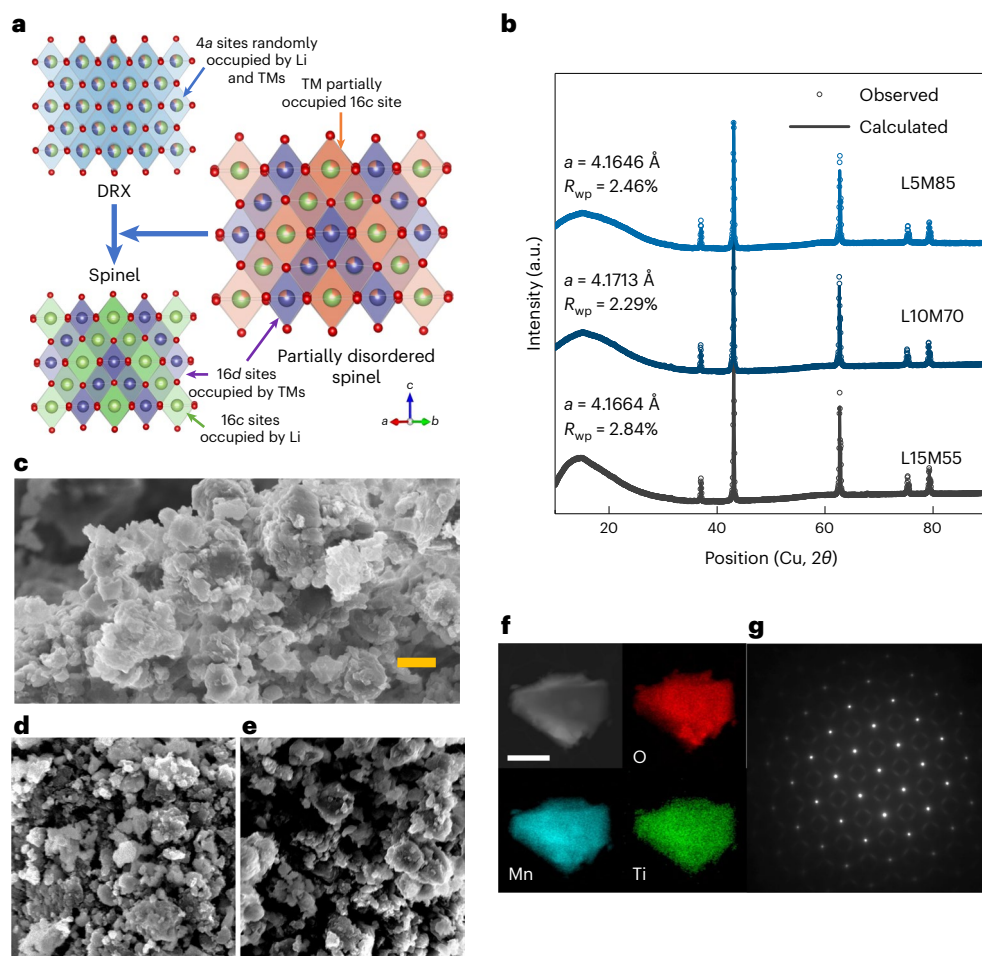


Fig. 1 | Characterization of the as-synthesized L5M85, L10M70 and L15M55. **a**, The partially disordered spinel phase as an intermediate between the DRX and fully ordered spinel structures. **b**, XRD patterns of L5M85, L10M70 and L15M55, refined based on the rock salt structure. The lattice parameter (a) and weighted

profile R factor (R_{wp}) are shown in the figure. **c–e**, SEM images of L5M85 (**c**), L10M70 (**d**) and L15M55 (**e**) after shaker milling with carbon (scale bar = 500 nm). **f**, STEM image and EDS mapping of the elements O, Mn and Ti in as-synthesized L5M85 (scale bar = 500 nm). **g**, SAED pattern of as-synthesized L5M85.

by the increasing difference between the average charge and discharge voltages, even though the mean value of them remains stable (Supplementary Fig. 2).

Electrochemical and structural characterization of L5M85

When cycling between 1.5 and 4.8 V, the initial capacity of L5M85 grows from 172 mAh g^{-1} (specific energy of 499 Wh kg^{-1}) to 270 mAh g^{-1} (specific energy of 777 Wh kg^{-1}) after 20 cycles (Fig. 3a). The voltage profile is flattened near -4 V and 3 V, which we attribute to the Li^+ insertion into 8a sites and 16c sites. The low voltage capacity near 1.7 V is attributed to insertion into 8a sites that face share with filled octahedral sites³⁴. We found that this capacity increase is also accompanied by an increase in rate performance. Supplementary Fig. 3 shows a comparison of the rate performance of L5M85 during the first and 20th cycle. While pristine L5M85 delivers only 52 mAh g^{-1} when cycled at 500 mA g^{-1} (32.3% of that at 20 mA g^{-1}), after 20 cycles, 130 mAh g^{-1} is obtained on discharge at 500 mA g^{-1} (48.7% of that at 20 mA g^{-1}).

Galvanostatic measurements within other voltage windows were also performed for L5M85 (Fig. 3b). When cycling between 1.5 and 5 V, 288.6 mAh g^{-1} is achieved at the 23rd cycle, with 85% of this capacity retained at cycle 100. The most stable cycling was achieved when cycling between 2 and 4.8 V. A capacity of 200 mAh g^{-1} is retained at the 100th cycle, which is 91.6% of the highest capacity (218.1 mAh g^{-1}) recorded at the cycle 41.

Using ex situ XRD, we observed that the structure gradually evolves upon cycling (Supplementary Fig. 4). Rietveld refinement of synchrotron XRD data collected after the 20th cycle of L5M85 was used to better understand the structure of the in situ formed new phase and its relation to performance (Fig. 3c). A single-phase spinel model with $Fd-3m$ space group was used as a starting point for the refinement. Partial occupancy on both the 16c and 16d sites by TMs was allowed in the refinement, yielding a TM occupancy of 0.90 and 0.05 for 16d and 16c, respectively, confirming the partial disordering in the δ phase (Supplementary Table 5). Selective peak broadening was applied to Bragg peaks with an odd l index when performing Rietveld refinement³⁵. These peaks, associated with the in situ formed spinel-like environment, appear broader than the rock salt peaks and fit to a 5.7 nm coherence length for the δ ordering, considerably smaller than the fitted crystallite size of 86 nm. Consistent with recently published theory²⁶, we believe that the specific structural features are key to the material's performance. To evaluate the impact of Mn/Ti content on the level of cation disorder in the δ phase after 20 cycles, we performed Rietveld refinement on XRD patterns of L10Mn70 and L15M55 collected after the 20th cycle using the same protocol as used for L5M85. The results are shown in Supplementary Tables 6 and 7. With decreasing Mn content, the 16c occupancy increases from 0.05 to 0.17 for L10M70 and further to 0.30 for L15M55, which indicates an increasing cation disorder and decreasing spinel-type ordering. The in situ XRD data at the 20th cycle indicates that the cycled L5M85 lithiates through a

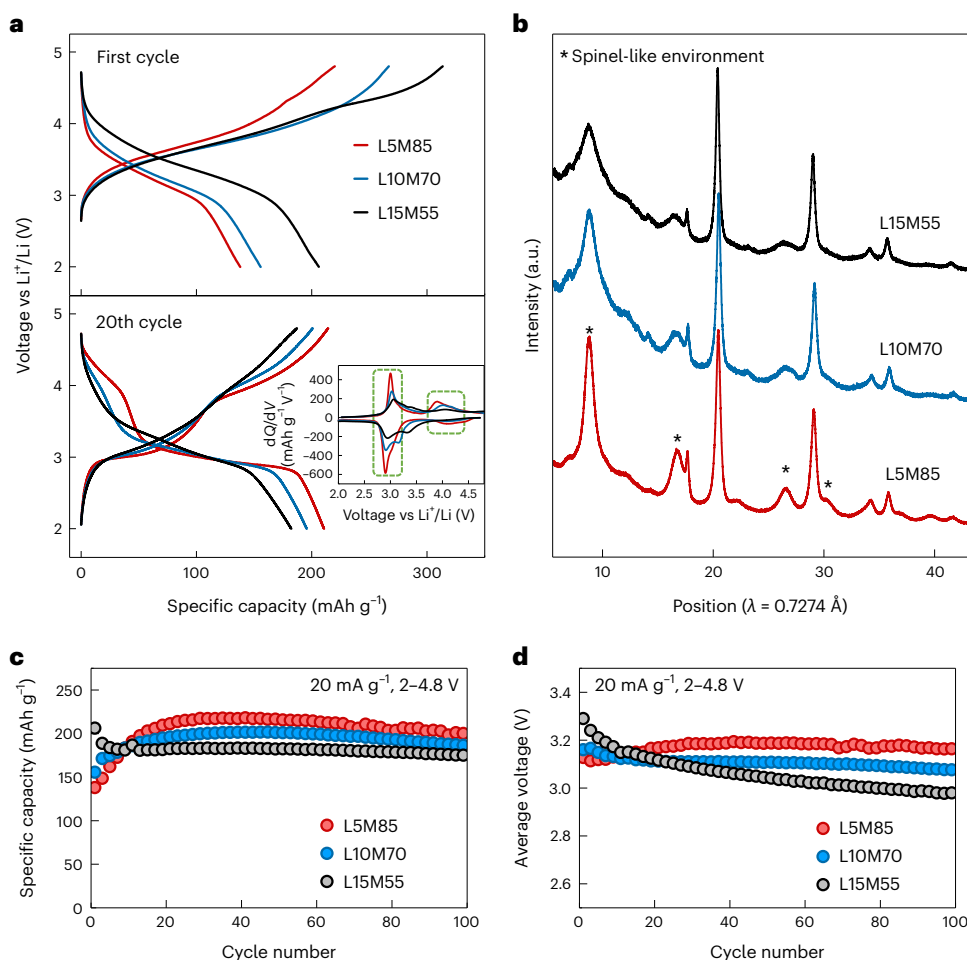


Fig. 2 | Electrochemical performance and structural characterization of L5M85, L10M70 and L15M55. **a**, Voltage profiles of L5M85, L10M70 and L15M55 for the first and the 20th cycles when cycled between 2 and 4.8 V at 20 mA g^{-1} . The inset shows the differential capacity (dQ/dV) curves of L5M85, L10M70 and

L15M55 for the 20th cycle. The squares in green highlight the formation of the 3-V and 4-V capacity regions. **b**, Synchrotron XRD patterns for ex situ samples discharged to 3.5 V during the 20th cycle. **c, d**, Capacity retention (**c**) and average voltage retention (**d**) of L5M85, L10M70 and L15M55 over the first 100 cycles.

solid-solution reaction in both the 4-V and 3-V regions (Supplementary Fig. 5). This finding indicates that the combination of a small amount of cation disorder and a small coherence length of spinel-like ordering can suppress most or all of the two-phase reaction during cycling.

Because of the low sensitivity of X-rays to Li, we also used solid-state nuclear magnetic resonance (ssNMR) spectroscopy to probe the evolution of ^7Li local environment upon cycling. We characterized ex situ samples extracted at the top of the charge on both the first and 20th cycle. The top of charge was used as those samples exhibit a similar average Mn valence (as confirmed by X-ray absorption spectroscopy (XAS) measurement shown in Supplementary Figs. 6–8) so that the impact of the Mn valence state on the ^7Li chemical shift could be minimized. Isotropic ^7Li spectra obtained using the projected magic-angle turning phase-adjusted sideband separation (pj-MATPASS) pulse sequence are compared in Fig. 3d. The broad ^7Li ssNMR resonance centred around 600 ppm results from the overlap of closely spaced and paramagnetically broadened signals due to a distribution of local ^7Li environments in the bulk cathode. On the other hand, the sharp signal at about 0 ppm corresponds to diamagnetic Li-containing impurity phases (LiF , Li_2CO_3 and/or $\text{Li}_2\text{O}/\text{LiOH}$), either originating from the synthesis (Supplementary Fig. 9) or formed upon electrolyte decomposition during cycling. The evolution of the full width at half maximum (FWHM) of the broad paramagnetic resonance is related to the distribution of ^7Li local environments in the cathode, whereby a smaller FWHM indicates a more ordered structure

(reduction in the number of local environments). The FWHM of the resonance obtained for the 20th charged sample is 410 ppm, smaller than that of the resonance obtained for the first charged sample (460 ppm). This suggests a narrower distribution of Li environments in the cathode upon cycling, supporting the formation of partially ordered environment from the cation-disordered lattice. The resonances observed in our ex situ cathode samples are still a lot broader than those obtained for ordered LiMn_2O_4 (line width $< 100 \text{ ppm}$)³⁶ and $\text{LiTi}_x\text{Mn}_{2-x}\text{O}_4$ spinel compounds (line width up to 300 ppm for the $x = 0.8$ composition)³⁷, suggesting that overall, a fairly disordered structure is maintained.

Although XRD and ssNMR provide bulk-sensitive information on the TM site occupancy and Li local environment, they do not provide much information as to how the new environment is accommodated in the cycled material. To gain further insights into the microstructure of the cycled L5M85 cathode, atomically resolved high angle annular dark field (HAADF) images were obtained on the ex situ sample collected at 3.5 V during the 20th discharge, as shown in Fig. 3e. The HAADF image taken along the $[110]$ zone axis clearly indicates the presence of spinel-like environments (Fig. 3g) with both $16d$ and $16c$ sites partially occupied by heavy cations (Ti or Mn) but with a very short coherence length ($\sim 5 \text{ nm}$). A more disordered environment (Fig. 3f) can also be observed in Fig. 3e. Such variations in local order are typical for partially disordered materials with small domain sizes^{24,25,38} or for disordered materials with strong SRO³⁵. Because the new local environment that forms upon cycling of L5M85 exhibits certain spinel-like features but

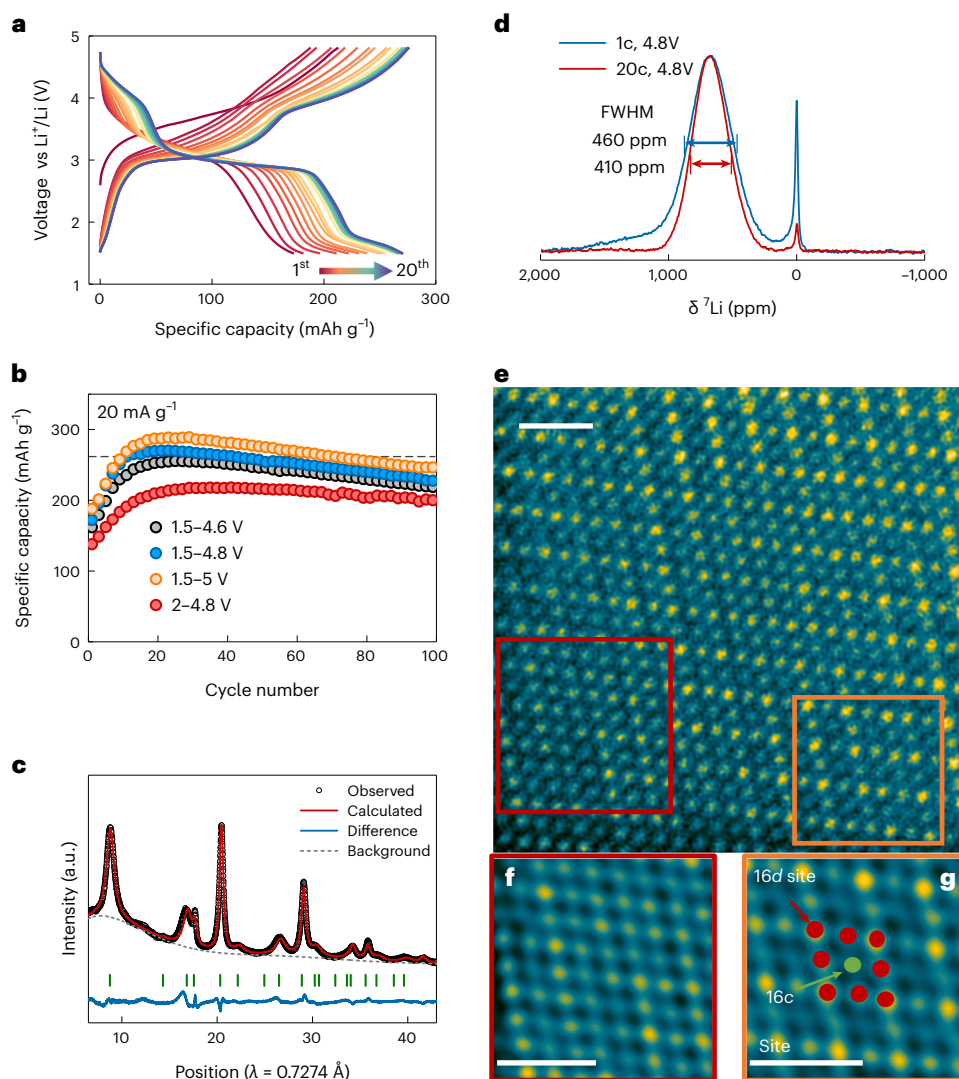


Fig. 3 | Electrochemical performance and structural characterization of LSM85. **a**, Electrochemical voltage profile of LSM85 cycled between 1.5 and 4.8 V for the first 20 cycles at room temperature. The black curve is the first cycle. From the second to 20th cycles, the colour gradually changes from green to red. **b**, Capacity retention of LSM85 over the first 100 cycles when cycled in different voltage windows at 20 mA g⁻¹. **c**, Rietveld refinement of synchrotron

X-ray diffraction for LSM85 discharged to 3.5 V at the 20th cycle. **d**, ⁷Li solid-state NMR spectra collected on ex situ samples charged to 4.8 V during the first and 20th cycles. **e**, STEM HAADF image of an ex situ cycled LSM85 sample discharged to 3.5 V during the 20th cycle. Scale bar = 1 nm. **f**, Magnified region of **e**, where a more disordered TM ordering is observed. Scale bar = 1 nm. **g**, Magnified region of **e**, where a more partially spinel-like ordering is observed. Scale bar = 1 nm.

is clearly not an ordered spinel phase (no two-phase 3-V plateau, existence of 16c/16d disorder, local fluctuations in order), we refer to this new structure as δ for short.

Discussion

Mn is a crucial element for the Li-ion industry as it is abundant, inexpensive, is associated with high redox voltage and its charged Mn⁴⁺ state is much more thermally stable than Ni⁴⁺ and Co⁴⁺. We show in this work that the high mobility of Mn cations can be used as an advantage to in situ create a stable cathode material with high energy density. Starting from an easily synthesized cation-disordered Li_{1.05}Mn_{0.85}Ti_{0.1}O₂ (LSM85) compound, transformation to the δ structure leads to a capacity of 288.6 mAh g⁻¹ with a specific energy of 826 Wh kg⁻¹ (Fig. 3b) and good rate capability (Supplementary Fig. 3b). This transformation into a high energy cathode material is accelerated with higher Mn and lower Ti content as evidenced from the comparison between Li_{1.05}Mn_{0.85}Ti_{0.1}O₂ (LSM85), Li_{1.1}Mn_{0.7}Ti_{0.2}O₂ (LIOM70) and Li_{1.15}Mn_{0.55}Ti_{0.3}O₂ (L15M55). Detailed structural characterizations, including synchrotron XRD,

ssNMR and high-resolution STEM analysis, indicate that an environment with lower symmetry forms that most closely resembles a partially disordered spinel-type cation ordering with low coherence length. As the structure of the δ phase is more ordered than the pristine DRX structure, the Li site energy distribution is narrower, which is confirmed by ⁷Li ssNMR (Fig. 3d). This leads to flattening of the voltage curve, enabling more capacity to be delivered in the same voltage window. In addition, the better Li⁺ percolation in the spinel-like δ phase improves the rate performance and increases the capacity³⁹. High-resolution STEM analysis indicates local variation in the extent of the δ phase ordering, which is likely closely linked to the non-uniform distribution of various TM species caused by cation SRO^{27,40–42} in the pristine DRX structure.

The δ phase reflects an optimal trade-off in terms of its degree of spinel-like local ordering. The presence of local spinel-like ordering is beneficial for Li transport as it enhances the O-TM percolation network^{24,25}, which we believe accounts for the capacity increase and rate performance improvement upon cycling (Supplementary Figs. 2 and 10). But the degree and coherence length of this ordering

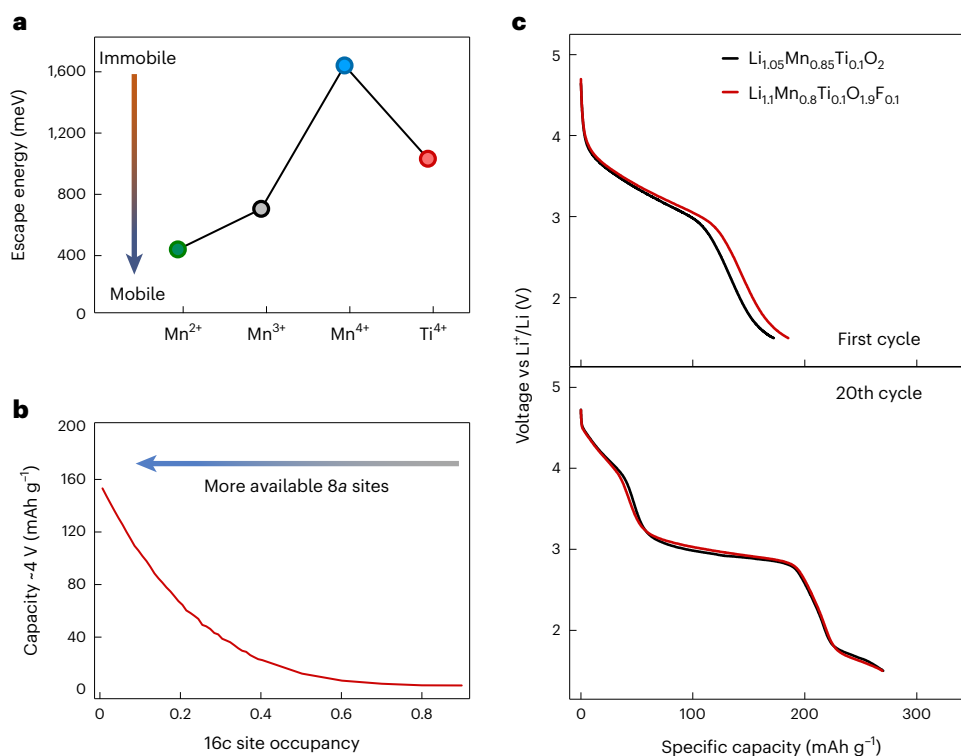


Fig. 4 | Kinetic analyses of DRX to δ phase transformation. **a**, Calculated escape energy from an octahedral site for Mn^{2+} , Mn^{3+} , Mn^{4+} and Ti^{4+} . **b**, Available $8a$ sites as a function of $16c$ site occupancy by a TM based on a spinel-like ordering. No face sharing between TM and Li is allowed. **c**, Voltage profiles of $\text{Li}_{1.05}\text{Mn}_{0.85}\text{Ti}_{0.1}\text{O}_2$ and $\text{Li}_{1.1}\text{Mn}_{0.8}\text{Ti}_{0.1}\text{O}_{1.9}\text{F}_{0.1}$ at the first and 20th cycles.

remains limited so that, unlike in a regular well-ordered spinel, no detrimental two-phase reaction takes place at 3 V. It is these structural features that unlock the full theoretical capacity of Mn-based cathodes. Recent work indeed identified that $16c/16d$ disorder enhances solid-solution behaviour around 3 V by creating more accessible environments for Li on tetrahedral and octahedral sites to be in a face-sharing configuration²⁶ and that new Li migration channels are created by the disorder⁴³.

In Supplementary Fig. 11, we show that high-Mn content DRX phases indeed have a driving force to form spinel-like order but that this driving force can be moderated by an increase in Ti content (Supplementary Notes 3 and 4). To better understand the kinetics of the DRX to δ structure change, we investigated in more detail the role of Mn and Ti mobility. It has been demonstrated in previous work that the tendency for TM migration is largely controlled by its electronic structure¹⁸. TM species with a small crystal field stabilization energy difference between octahedral coordination and tetrahedral coordination usually have small migration barriers and are thus prone to migration. Figure 4a shows the escape energy for Mn^{2+} , Mn^{3+} , Mn^{4+} and Ti^{4+} in a Li excess rock salt configuration, calculated using nudged-elastic band (NEB) density functional theory, as described in the Methods section. The migration assumes the presence of a trivacancy for the TM with higher charge state (Mn^{3+} , Mn^{4+} , Ti^{4+}) and a divacancy for Mn^{2+} . For comparison, the trivacancy-based Mn^{2+} migration is shown, along with the energy profiles of the other TM migration in Supplementary Fig. 12. Mn^{4+} and Ti^{4+} show very high escape energies of $\sim 1,000$ meV or higher, indicating that they are highly likely to remain immobile during cycling. However, reducing Mn^{4+} to Mn^{3+} or Mn^{2+} decreases the barrier to ~ 700 meV and ~ 400 meV, respectively. Therefore, the Mn ions are mainly responsible for the TM reordering to form the δ phase. This is consistent with our experimental observations that the DRX to δ phase transformation is more pronounced in Mn-rich and Ti-poor compositions.

Whereas the high mobility of Mn promotes the transformation, it is the immobile cations that determine the final structure of the δ phase and are responsible for its solid-solution behaviour. In the initial structure, all the cations randomly occupy the octahedral sites, which in spinel nomenclature would correspond to an equal distribution on $16c$ and $16d$ sites ($Fd\bar{3}m$ space group). As the material evolves with cycling, the mobile cations can rearrange towards local $16d$ order (spinel-like order), but the remaining immobile cations on the $16c$ sites cannot rearrange and create the partial disorder that prevents the formation of complete and long-range spinel order and leads to the very short coherence length of the spinel-like environments. The lack of coherence between local spinel environments and the partial disorder are what prevents the collective first-order transition responsible for the 3-V plateau in ordered spinel. Thus, the role of Ti^{4+} as an immobile cation is critical in the formation of the high performance δ phase.

The presence of site disorder is reflected in the voltage profile of the δ phase. The $16c$ sites (normally vacant in spinel) face share with $8a$ sites, which are normally occupied by Li^+ in spinel and are responsible for their electrochemical activity at ~ 4 V. When the $16c$ sites are occupied due to the partial cation disorder, the face-sharing $8a$ sites cannot be occupied by Li^+ due to the high energy of such configuration⁴⁴, leading to a shortening of the 4-V plateau. Indeed, while an ordered spinel has the same capacity in both the 4-V and 3-V plateau, the δ phase exhibits higher capacity in the 3-V region than in the 4-V region (Fig. 2a). With increasing Ti content (for example, compare L15M55 with L5M85), the electrochemical performance after 20 cycles shows less capacity in the ~ 4 -V region, which lowers energy density. Hence, the Ti content should be controlled to tune the disorder of the δ phase and optimize the electrochemical performance.

We computationally evaluated the theoretical capacity expected to be delivered at the 4-V plateau as a function of $16c$ site occupancy, with the results shown in Fig. 4b. The simulation demonstrates that

increasing TM occupancy of 16c sites decreases the amount of 8a sites available for Li occupation, in line with the decrease in capacity at the 4-V region seen in Fig. 2a. As the only fully immobile TM species within the entire operating voltage range, Ti^{4+} plays a critical role in blocking the system from complete transformation to an ordered spinel by maintaining a certain level of 16c site occupancy. As a consequence, δ phases with less Ti are expected to deliver more capacity at 4 V region, which is consistent with the electrochemical data shown in Fig. 2a.

To further test our hypothesis regarding the effect of immobile Ti^{4+} on the voltage profile, we synthesized $\text{Li}_{1.1}\text{Mn}_{0.8}\text{Ti}_{0.1}\text{O}_{1.9}\text{F}_{0.1}$ (L10M80F10), which contains the same Ti content but different Mn, Li and F content as L5M85 (Supplementary Note 5). Although the voltage profiles of these two materials differ in the first cycle, they become nearly identical in the 20th cycle, particularly in the 4-V plateau region (Fig. 4c). A similar comparison between $\text{Li}_{1.1}\text{Mn}_{0.75}\text{Ti}_{0.15}\text{O}_{1.95}\text{F}_{0.05}$ (Li10M75F5) and $\text{Li}_{1.15}\text{Mn}_{0.7}\text{Ti}_{0.15}\text{O}_{1.85}\text{F}_{0.15}$ (L15M70F15), which both contain 0.15 Ti per formula unit (f.u.), also shows that the two compositions demonstrate similar voltage profiles at the 20th cycle (Supplementary Fig. 13d) despite distinct initial voltage profiles. In contrast, the voltage profiles of L10M70 and L15M70F15, which both contain 0.7 Mn per f.u. but have different Ti content, remain different at the 20th cycle (Supplementary Fig. 13e). These control experiments are consistent with our understanding of the formation of the δ phase and confirm that the Ti content, rather than the Mn content, decides the structure of the δ phase and the shape of the voltage profile after transformation. One would fully expect that this result would remain valid for other immobile cations in DRX compounds, for example, Nb^{5+} (refs. 45–47) and even in layered NMCs. As LMR-NMCs also show transformation to a spinel-like structure during cycling when Mn is reduced by irreversible oxygen redox⁴⁸, the immobility of Co, Ni and Mn^{4+} impede the formation of accessible 8a sites, thus lowering the average voltage by only presenting 3-V activity without the 4-V region. Properly adjusting the ratio of immobile TMs may be a future direction to inhibit voltage decay of LMR-NMCs. Therefore, although the transformation to a spinel-like structure is inevitable in most Mn-rich cathodes, the voltage degradation can be avoided by forming a 4-V region.

We note that the presence of immobile Ti^{4+} is crucial for suppressing the detrimental two-phase reaction and Mn^{3+} -induced collective Jahn–Teller distortion upon cycling as it perturbs the long-range ordering and concomitant collective Li migration behaviour around 3 V (refs. 2–4). As a result, the δ phase L5M85 demonstrates a pure solid-solution behaviour upon cycling even though pseudo plateaus appear (Supplementary Fig. 5). These pseudo plateaus arise from the partial ordering in the material, which flatten the voltage curve as compared to a traditional more disordered DRX compound^{24,25}.

We would like to emphasize a trade-off when deciding the Ti content in the pristine DRX cathodes. Whereas maintaining sufficient Ti content is vital to retain enough disorder to suppress the two-phase reaction at 3 V, reducing it increases the available 8a sites in the δ phase, which leads to more capacity in the 4-V area and increases the average voltage and specific energy. A Ti content at or slightly larger than what is minimally required to suppress the two-phase reaction may be desired to achieve the highest voltage and specific energy.

In summary, we have demonstrated that high and stable capacity can be achieved in Mn-rich DRX compounds by allowing them to transform to a partially disordered spinel. Ti is used to regulate the driving force to spinel and control the coherence length over which spinel ordering occurs. This limited coherence length and the 16c/16d site disorder are critical to prevent the inhomogeneous two-phase reaction that is detrimental in a well-ordered spinel. This unique δ phase has a high capacity of 288.6 mAh g^{-1} and displays good rate capability. This performance, combined with the low cost of Mn and Ti-based oxide precursors, make it an excellent candidate to create abundant and inexpensive Li-ion energy storage materials.

Conclusions

Designing high-capacity Mn-based cathode materials is critical to address the resource challenges associated with Li-ion batteries. We have demonstrated that the group of Mn-rich DRX cathode materials achieve high reversible capacity and energy without voltage drop during an in situ transformation to a δ phase with partial spinel-like cation ordering and short coherence length. Immobile TMs, such as Ti^{4+} , play an important role in regulating the driving force for the transformation and controlling the structure of the δ phase. This transformed material shows an appealing pathway towards earth-abundant cathode materials for the Li-ion battery industry. Future improvements may be possible by reducing the immobile cation content to increase the length of the 4-V plateau and by replacing Mn with a multi-electron redox centre, for example, Cr, to increase the theoretical TM redox capacity.

Methods

Synthesis

$\text{Li}_{1.05}\text{Mn}_{0.85}\text{Ti}_{0.1}\text{O}_2$ (L5M85), $\text{Li}_{1.1}\text{Mn}_{0.7}\text{Ti}_{0.2}\text{O}_2$ (L10M70), $\text{Li}_{1.15}\text{Mn}_{0.55}\text{Ti}_{0.3}\text{O}_2$ (L15M55), $\text{Li}_{1.2}\text{Mn}_{0.4}\text{Ti}_{0.4}\text{O}_2$, $\text{Li}_{1.2}\text{Mn}_{0.5}\text{Ti}_{0.3}\text{O}_{1.9}\text{F}_{0.1}$ (L20M50), $\text{Li}_{1.2}\text{Mn}_{0.7}\text{Ti}_{0.1}\text{O}_{1.9}\text{F}_{0.1}$ (L20M70), $\text{Li}_{1.1}\text{Mn}_{0.75}\text{Ti}_{0.15}\text{O}_{1.95}\text{F}_{0.05}$ (Li10M75F5), $\text{Li}_{1.1}\text{Mn}_{0.8}\text{Ti}_{0.1}\text{O}_{1.9}\text{F}_{0.1}$ (Li10M80F10) and $\text{Li}_{1.15}\text{Mn}_{0.7}\text{Ti}_{0.15}\text{O}_{1.85}\text{F}_{0.15}$ (Li15M70F15) were synthesized by a solid-state synthesis method. Li_2CO_3 (Sigma, 99.99%), Mn_2O_3 (Alfa Aesar, 99%), TiO_2 (Alfa Aesar, 99%), MnO_2 (Alfa Aesar, 99.9%) and LiF (Alfa Aesar, 99.99%) were used as precursors. Three grams of precursors, except for Li_2CO_3 , was stoichiometrically added into a 50 ml stainless steel jar with 5 ml ethanol and 10 mm stainless steel balls. Ten percent more Li_2CO_3 was added to compensate for possible loss during synthesis. The precursors were mixed in a Retsch PM200 planetary ball mill at a rate of 250 r.p.m. for 12 h. The mixed precursors were dried in a 70 °C oven overnight before being grinded with a mortar and pestle and pelletized into a pellet. The 500 mg pellet was sintered in a tube furnace at 1,100 °C for 20 min under argon gas flow.

Electrochemistry

To make the cathode film, 280 mg of the as-synthesized active materials and 80 mg Super C65 carbon black (Timcal) were mixed in a zirconia jar and sealed in an Ar-filled glovebox. The mixture was shaker milled for 1 h using a SPEX 8000 M miller. The composite powder was mixed manually with PTFE (Dupont) in a 9:1 ratio with a mortar and pestle. The mixed composite was then rolled into free-standing thin films and cut with a 5/16-inch-diameter punch. The electrolyte used is 1 M LiPF₆ in ethylene carbonate and dimethyl carbonate solution (volume ratio 1:1, Sigma-Aldrich). Glass microfibers (Whatman) were cut with a 16 mm punch and used as separators. Li (FMC) round metal foil (7/16 inches in diameter) was used as anode. After sealing the coin cells (CR2032), they rested for 6 h before being tested on an Arbin battery cycler at 25 °C. All cathode films fabrication and coin cell assembly were operated in an Ar-filled glovebox.

Characterization

Synchrotron XRD patterns were measured at Beamline 2-1 of the Stanford Synchrotron Radiation Lightsource and Beamline I-11 at the DIAMOND Light Source. The ex situ cathode films were prepared by mixing the active materials, Super C65 and PVDF in at a weight ratio of 7:2:1. The cathode film was cycled at 20 mA g^{-1} current density, followed by equilibrating at a certain voltage for 6 h. The cells were then disassembled and the cathode film was washed with diethyl carbonate (DEC). All the synchrotron refinements were carried out using the TOPAS software package. A single-phase spinel structure model was used when refining the XRD patterns of cycled samples. The reflections with odd l index, which are generated by the spinel-type cation ordering, show broader peaks than those with even l index, which are generated by the face centred cubic cation and anion framework. Therefore, we applied the selective peak broadening to capture the broad peaks with odd l index, as applied in a previous publication on DRX cathode³⁵. The broadening factor

applied to the group of selected peaks is directly related to the size of spinel-like ordering, yielding an estimated coherence length for such environment (5.7 nm). SEM images were collected using a Zeiss Gemini Ultra-55 Analytical Field Emission SEM. In situ XRD was conducted on a Bruker D8 ADVANCE X-ray diffractometer with Mo K α radiation. A home-made in situ cell with a Be window was cycled at 20 mA g⁻¹ between 1.5 and 4.8 V using a Maccor potentiostat. The XRD patterns were collected in the 2 θ ranging from 14° to 29° every 1 h at room temperature.

Transmission electron microscopy

To prepare the ex situ samples for TEM, 350 mg of the as-synthesized active materials and 100 mg of Super C65 were ball milled at 250 r.p.m. for 6 h in a stainless steel jar sealed in an Ar-filled glovebox using a Retsch PM200 planetary ball mill. The composite was manually mixed with PTFE with a mortar and pestle in a ratio of 9:1. The composite was then rolled into cathode thin film. The electrode films were cycled in coin cells on Arbin battery cycler at 25 °C to different SOC and hold at a certain voltage for 6 h to reach equilibrium. The cycled cathode particles were dispersed in hexane with ultrasonic cell disruptor and dispensed onto TEM lacey carbon grids. TEM imaging and diffraction were performed on an aberration-corrected Titan 80–300 scanning/transmission electron microscope (S/TEM) operated at 300 kV. The electron diffraction patterns were collected with a selected area diffraction (SEAD) aperture of 10 μ m inserted. STEM HAADF imaging was performed on an aberration-corrected Themis Z scanning/transmission electron microscope (S/TEM) operated at 300 kV. The convergence semi-angle was 20.6 mrad. Signals for semi-angles spanning from 68 to 280 mrad were collected for STEM HAADF imaging. The EDS data were collected using a Super-X detector inside Themis Z STEM, and analysis was performed using the software ‘velox’, where the overlapped peaks were deconvolved using the stored standard reference spectra and a multiple linear least-squares fitting method.

Ex situ Mn K-edge X-ray absorption spectroscopy

Ex situ XAS measurements at the Mn and Ti K-edge were performed in a transmission mode at Beamline 20-BM-B of the Advanced Photon Source, Argonne National Laboratory. To select the incident beam energy, a Si (111) monochromator was applied. An Rh-coated mirror was used to get harmonic rejection. The electrode films were cycled in coin cells to different SOC and held at a certain voltage for 6 h. The cells were disassembled in an Ar-filled glovebox, and the films were washed with DEC. The energy calibration was accomplished by simultaneously measuring the spectra of Mn and Ti metal foil. Data processing was carried out by Athena software⁴⁹.

Mapping of resonant inelastic X-ray scattering

Mapping of resonant inelastic X-ray scattering (mRIXS) of O K-edge and Mn L-edge was measured in the in situ resonant inelastic X-ray scattering end station at Beamline 8.0.1 of the Advanced Light Source⁵⁰ at Lawrence Berkeley National Laboratory. The beam spot size is about 25 \times 100 μ m². Mapping data were collected by the ultrahigh efficiency modular spectrometer⁵¹, with an excitation energy step of 0.2 eV. The resolution of the excitation energy is 0.35 eV and that of the emission energy is 0.25 eV. The ex situ samples were electrode films, composed of active materials, carbon black and PTFE in a weight ratio of 70:20:10. The electrode films were charged or discharged to a certain state of charge in a coin cell at 20 mA g⁻¹ and held at that voltage for 6 h. The cells were disassembled, and the films were washed with DEC in an Ar-filled glovebox. Final 2D maps were achieved via multi-step data processing including normalization to beam flux and collecting time, integration and combination and so on, which has been elaborated on in previous work²⁵.

Solid-state nuclear magnetic resonance spectroscopy

⁷Li ssNMR data collected on L5M85 use a Bruker Biospin wide bore magnet ($B_0 = 2.35$ T, 100 MHz for ¹H), equipped with a DMX 500 MHz console and a custom-made 1.3 mm X-broadband magic angle spinning

probe tuned to ⁷Li (38.88 MHz). ⁷Li ssNMR data collected on L20M50 and L20M70 used a Bruker Avance III magnet ($B_0 = 4.7$ T, 200 MHz for ¹H), equipped with a Bruker 1.3 mm double-resonance probe tuned to ⁷Li (77.75 MHz).

To limit sample exposure to air and moisture, materials were packed in zirconia rotors in an Ar-filled glovebox, and all spectra were recorded under magic angle spinning at $\nu_R = 60$ kHz using dry nitrogen. ⁷Li NMR data were externally referenced against pure lithium fluoride (LiF, $\delta(^7\text{Li}) = -1$ ppm), which was also used for radiofrequency (RF) pulse calibration. Spectra were processed using Topspin 3.6.5, and lineshape analysis was carried out using DMfit software⁵².

⁷Li pj-MATPASS⁵³ pure isotropic spectra were obtained using a 90° RF pulse of 0.43 μ s (L5M85) or 0.6 μ s (L20M50 and L20M70), averaging 2,000 (L5M85) or 8,000 (L20M50 and L20M70) transients with a recycle delay of 50 ms (L5M85) or 40 ms (L20M50 and L20M70). A ⁷Li quantitative NMR spectrum was obtained using a rotor synchronized spin-echo sequence using 90° and 180° RF pulses of 0.43 and 0.86 μ s, respectively. A total of 256 transients were averaged with a recycle delay of 1 s, which was enough to reach full relaxation of all ⁷Li signals.

Density functional theory calculations

First-principles density functional theory (DFT) calculations were performed to obtain an accurate description of the structural energies and oxidation states of different cathode materials. All the calculations were performed using the projector-augmented wave method⁵⁴ as implemented in the Vienna ab initio Simulation Package⁵⁵. The meta generalized gradient approximation (meta-GGA) functional strongly constrained and appropriately normed (SCAN) has been used to obtain a more accurate description of phase stability^{56–58}. For all calculations, a reciprocal space discretization of 25 K-points per Å^{-3} was applied, and the convergence criteria were set as 10⁻⁶ eV for electronic loops and 0.02 eV Å^{-1} for ionic loops. All calculations were performed with spin polarization and initialized in a ferromagnetic spin state.

For generating structures with γ -LiFeO₂-like ordering and spinel-like ordering, ion substitution was performed on a γ -LiFeO₂ and LT-LiCoO₂ model. Enumeration is then performed for obtaining the five cation configurations with the lowest Ewald energy for DFT calculation. The lowest energy structure at each composition is selected to calculate the thermodynamic driving force. To make sure we capture the largest thermodynamic driving force, all energetic difference between structures with γ -LiFeO₂-type ordering (E_V) and spinel-type ordering (E_S) values are calculated at spinel composition, for example, cation/anion = 3/4. This is achieved by removing 0.5 Li per f.u. from the compound.

Nudged-elastic band calculations

The nudged-elastic band (NEB) method^{59,60} was used with DFT to calculate the migration barriers of transition metals from octahedral sites to neighbouring tetrahedral sites. We used the GGA functional with a Hubbard U correction of 3.9 eV (refs. 61,62) due to the higher computing cost of SCAN and converge forces to 0.05 eV Å^{-1} . To enforce Mn valence to 2⁺, 3⁺ and 4⁺ when calculating Mn migration barriers, a homogeneous background charge is applied⁶³. To minimize the number of additional electrons contributing to the background charge, calculations are performed on a low-energy rock salt with low Mn composition (Li₃₃Ti₁₈Mn₆O₆₀).

The migration of the transition metal along the diffusion pathway is discretized into five images between the initial and final states. For the transition metals with higher oxidation state (Mn³⁺, Mn⁴⁺, Ti⁴⁺), we assume migration via a trivacancy mechanism because single vacancy and divacancy mechanisms would require face sharing of the transition metal with other cations in the activated state. The Mn²⁺ migration calculation is performed with both a divacancy and a trivacancy mechanism due to its lower charge. From a converged NEB calculation, the escape energy is calculated as the difference between the maximum and minimum energies along the migration path.

Data availability

All data generated and analysed during this study are included in the published article and its Supplementary Information. Source data are provided with this paper.

References

- Huang, Y. et al. Lithium manganese spinel cathodes for lithium-ion batteries. *Adv. Energy Mater.* **11**, 2000997 (2020).
- Thackeray, M. M. et al. Spinel electrodes from the Li–Mn–O system for rechargeable lithium battery applications. *J. Electrochem. Soc.* **139**, 363 (1992).
- David, W. I. F., Thackeray, M. M., De Picciotto, L. A. & Goodenough, J. B. Structure refinement of the spinel-related phases $\text{Li}_2\text{Mn}_2\text{O}_4$ and $\text{Li}_{0.2}\text{Mn}_2\text{O}_4$. *J. Solid State Chem.* **67**, 316–323 (1987).
- Thackeray, M. M., David, W. I. F., Bruce, P. G. & Goodenough, J. B. Lithium insertion into manganese spinels. *Mater. Res. Bull.* **18**, 461–472 (1983).
- Zubair, M. et al. Stabilizing structure and voltage decay of lithium-rich cathode materials. *Ceram. Int.* **49**, 8936–8944 (2022).
- Zhang, X. et al. Bulk oxygen stabilization via electrode-electrolyte interphase tailored surface activities of Li-rich cathodes. *Adv. Energy Mater.* **13**, 2202929 (2022).
- Zeng, W. et al. Single-crystal Li-rich layered cathodes with suppressed voltage decay by double-layer interface engineering. *Energy Storage Mater.* **54**, 651–660 (2022).
- Yang, Z. et al. Multi-dimensional correlation of layered Li-rich Mn-based cathode materials. *Energy Mater.* **2**, 200006 (2022).
- Hua, W. et al. Lithium/oxygen incorporation and microstructural evolution during synthesis of Li-rich layered Li $[\text{Li}_{0.2}\text{Ni}_{0.2}\text{Mn}_{0.6}] \text{O}_2$ oxides. *Adv. Energy Mater.* **9**, 1803094 (2019).
- Gao, S. et al. The role of various components of transition metal layer on the properties of Li-rich cathode $\text{Li}_{1.2}[\text{M}_{0.4}\text{Mn}_{0.4}]\text{O}_2$ (M = Ni, Co, $\text{Ni}_{1/2}\text{Mn}_{1/2}$ and Fe). *J. Electrochem. Soc.* **164**, A3824 (2017).
- Zheng, J. et al. Structural and chemical evolution of Li-and Mn-rich layered cathode material. *Chem. Mater.* **27**, 1381–1390 (2015).
- Zheng, J. et al. Mitigating voltage fade in cathode materials by improving the atomic level uniformity of elemental distribution. *Nano Lett.* **14**, 2628–2635 (2014).
- Gu, M. et al. Formation of the spinel phase in the layered composite cathode used in Li-ion batteries. *ACS Nano* **7**, 760–767 (2013).
- Armstrong, A. R. & Bruce, P. G. Synthesis of layered LiMnO_2 as an electrode for rechargeable lithium batteries. *Nature* **381**, 499–500 (1996).
- Capitaine, F., Gravereau, P. & Delmas, C. A new variety of LiMnO_2 with a layered structure. *Solid State Ion.* **89**, 197–202 (1996).
- Sathiyaraj, M. et al. Origin of voltage decay in high-capacity layered oxide electrodes. *Nat. Mater.* **14**, 230–238 (2015).
- Hua, W. et al. Structural insights into the formation and voltage degradation of lithium-and manganese-rich layered oxides. *Nat. Commun.* **10**, 5365 (2019).
- Reed, J. & Ceder, G. Role of electronic structure in the susceptibility of metastable transition-metal oxide structures to transformation. *Chem. Rev.* **104**, 4513–4534 (2004).
- Reed, J., Ceder, G. & Van Der Ven, A. Layered-to-spinel phase transition in Li_xMnO_2 . *Electrochem. Solid State Lett.* **4**, A78 (2001).
- Freire, M. et al. A new active Li–Mn–O compound for high energy density Li-ion batteries. *Nat. Mater.* **15**, 173–177 (2016).
- Li, L. et al. Fluorination-enhanced surface stability of disordered rocksalt cathodes. *Adv. Mater.* **34**, e2106256 (2022).
- Ahn, J. et al. Exceptional cycling performance enabled by local structural rearrangements in disordered rocksalt cathodes. *Adv. Energy Mater.* **12**, 2200426 (2022).
- Li, L. et al. Fluorination-enhanced surface stability of cation-disordered rocksalt cathodes for Li-ion batteries. *Adv. Funct. Mater.* **31**, 2101888 (2021).
- Cai, Z. et al. Realizing continuous cation order-to-disorder tuning in a class of high-energy spinel-type Li-ion cathodes. *Matter* **4**, 3897–3916 (2021).
- Ji, H. W. et al. Ultrahigh power and energy density in partially ordered lithium-ion cathode materials. *Nat. Energy* **5**, 213–221 (2020).
- Chen, T., Yang, J., Barroso-Luque, L. & Ceder, G. Removing the two-phase transition in spinel LiMn_2O_4 through cation disorder. *ACS Energy Lett.* **8**, 314–319 (2022).
- Ji, H. et al. Hidden structural and chemical order controls lithium transport in cation-disordered oxides for rechargeable batteries. *Nat. Commun.* **10**, 592 (2019).
- Lee, J. et al. Unlocking the potential of cation-disordered oxides for rechargeable lithium batteries. *Science* **343**, 519–522 (2014).
- Assat, G. & Tarascon, J.-M. Fundamental understanding and practical challenges of anionic redox activity in Li-ion batteries. *Nat. Energy* **1**, 373–386 (2018).
- Zheng, J. et al. Li-and Mn-rich cathode materials: challenges to commercialization. *Adv. Energy Mater.* **7**, 1601284 (2017).
- Eum, D. et al. Voltage decay and redox asymmetry mitigation by reversible cation migration in lithium-rich layered oxide electrodes. *Nat. Mater.* **19**, 419–427 (2020).
- Huang, T. Y., Crafton, M. J., Yue, Y., Tong, W. & McCloskey, B. D. Deconvolution of intermixed redox processes in Ni-based cation-disordered Li-excess cathodes. *Energy Environ. Sci.* **14**, 1553–1562 (2021).
- Crafton, M. J., Yue, Y., Huang, T. Y., Tong, W. & McCloskey, B. D. Anion reactivity in cation-disordered rocksalt cathode materials: the influence of fluorine substitution. *Adv. Energy Mater.* **35**, 2001500 (2020).
- Jobst, N. M. et al. Dynamic structure evolution of extensively delithiated high voltage spinel $\text{Li}_{1+x}\text{Ni}_{0.5}\text{Mn}_{1.5}\text{O}_4$ $x < 1.5$. *J. Am. Chem. Soc.* **145**, 4450–4461 (2023).
- Jones, M. A. et al. Short-range ordering in a battery electrode, the ‘cation-disordered’rocksalt $\text{Li}_{1.25}\text{Nb}_{0.25}\text{Mn}_{0.5}\text{O}_2$. *Chem. Commun.* **55**, 9027–9030 (2019).
- Grey, C. P. & Lee, Y. J. Lithium MAS NMR studies of cathode materials for lithium-ion batteries. *Solid State Sci.* **5**, 883–894 (2003).
- Pigliapochi, R. et al. Structural characterization of the Li-ion battery cathode materials $\text{LiTi}_x\text{Mn}_{2-x}\text{O}_4$ ($0.2 \leq x \leq 1.5$): a combined experimental ^7Li NMR and first-principles study. *Chem. Mater.* **30**, 817–829 (2018).
- Lee, E. et al. Nanocomposite engineering of a high-capacity partially ordered cathode for Li-ion batteries. *Adv. Mater.* **35**, e2208423 (2023).
- Urban, A., Lee, J. & Ceder, G. The configurational space of rocksalt-type oxides for high-capacity lithium battery electrodes. *Adv. Energy Mater.* **4**, 1400478 (2014).
- Kan, W. H. et al. Understanding the effect of local short-range ordering on lithium diffusion in $\text{Li}_{1.3}\text{Nb}_{0.3}\text{Mn}_{0.4}\text{O}_2$ single-crystal cathode. *Chem* **4**, 2108–2123 (2018).
- Diaz-Lopez, M. et al. Li trapping in nanolayers of cation ‘disordered’rock salt cathodes. *J. Mater. Chem. A* **10**, 17415–17423 (2022).
- Diaz-Lopez, M. et al. Reversible densification in nano- Li_2MnO_3 cation disordered rock-salt Li-ion battery cathodes. *J. Mater. Chem. A* **8**, 10998–11010 (2020).
- Yang, J. H. & Ceder, G. Activated internetwork pathways in partially-disordered spinel cathode materials with ultrahigh rate performance. *Adv. Energy Mater.* **13**, 2202955 (2022).

44. Zhang, W. et al. Kinetic pathways of ionic transport in fast-charging lithium titanate. *Science* **367**, 1030–1034 (2020).
45. Wang, R. et al. A disordered rock-salt Li-excess cathode material with high capacity and substantial oxygen redox activity: $\text{Li}_{1.25}\text{Nb}_{0.25}\text{Mn}_{0.5}\text{O}_2$. *Electrochem. Commun.* **60**, 70–73 (2015).
46. Chen, D. et al. Role of redox-inactive transition-metals in the behavior of cation-disordered rocksalt cathodes. *Small* **16**, e2000656 (2020).
47. Ahn, J., Chen, D. & Chen, G. A fluorination method for improving cation-disordered rocksalt cathode performance. *Adv. Energy Mater.* **10**, 2001671 (2020).
48. Liu, Q. et al. High-performance lithium-rich layered oxide material: effects of preparation methods on microstructure and electrochemical properties. *Materials* **13**, 334 (2020).
49. Ravel, B. & Newville, M. ATHENA, ARTEMIS, HEPHAESTUS: data analysis for X-ray absorption spectroscopy using IFEFFIT. *J. Synchrotron Radiat.* **12**, 537–541 (2005).
50. Qiao, R. et al. High-efficiency in situ resonant inelastic x-ray scattering (iRIXS) endstation at the Advanced Light Source. *Rev. Sci. Instrum.* **88**, 033106 (2017).
51. Chuang, Y.-D. et al. Modular soft X-ray spectrometer for applications in energy sciences and quantum materials. *Rev. Sci. Instrum.* **88**, 013110 (2017).
52. Massiot, D. et al. Modelling one- and two-dimensional solid-state NMR spectra. *Magn. Reson. Chem.* **40**, 70–76 (2002).
53. Hung, I., Zhou, L., Pourpoint, F. D. R., Grey, C. P. & Gan, Z. Isotropic high field NMR spectra of Li-ion battery materials with anisotropy >1 MHz. *JACS* **134**, 1898–1901 (2012).
54. Kresse, G. & Joubert, D. From ultrasoft pseudopotentials to the projector augmented-wave method. *Phys. Rev. B* **59**, 1758 (1999).
55. Kresse, G. & Furthmüller, J. Efficient iterative schemes for ab initio total-energy calculations using a plane-wave basis set. *Phys. Rev. B* **54**, 11169 (1996).
56. Zhang, Y. et al. Efficient first-principles prediction of solid stability: towards chemical accuracy. *npj Comput. Mater.* **4**, 9 (2018).
57. Sun, J. et al. Accurate first-principles structures and energies of diversely bonded systems from an efficient density functional. *Nat. Chem.* **8**, 831–836 (2016).
58. Sun, J., Ruzsinszky, A. & Perdew, J. P. Strongly constrained and appropriately normed semilocal density functional. *Phys. Rev. Lett.* **115**, 036402 (2015).
59. Olsen, R., Kroes, G., Henkelman, G., Arnaldsson, A. & Jónsson, H. Comparison of methods for finding saddle points without knowledge of the final states. *J. Chem. Phys.* **121**, 9776–9792 (2004).
60. Sheppard, D., Terrell, R. & Henkelman, G. Optimization methods for finding minimum energy paths. *J. Chem. Phys.* **128**, 134106 (2008).
61. Kulik, H. J., Cococcioni, M., Scherlis, D. A. & Marzari, N. Density functional theory in transition-metal chemistry: a self-consistent Hubbard U approach. *Phys. Rev. Lett.* **97**, 103001 (2006).
62. Dudarev, S. L., Botton, G. A., Savrasov, S. Y., Humphreys, C. & Sutton, A. P. Electron–energy-loss spectra and the structural stability of nickel oxide: an LSDA+ U study. *Phys. Rev. B* **57**, 1505 (1998).
63. Chen, T., Sai Gautam, G. & Canepa, P. Ionic transport in potential coating materials for Mg batteries. *Chem. Mater.* **31**, 8087–8099 (2019).

Acknowledgements

This work was supported by the Assistant Secretary for Energy Efficiency and Renewable Energy, Vehicle Technologies Office under the Applied Battery Materials Program of the US Department of Energy (DOE) under contract number DE-AC02-05CH11231. Work at the Molecular Foundry was supported by the Office of Science, Office of Basic Energy Sciences of the US DOE under contract number DE-AC02-05CH11231. This research used resources of the Advanced

Photon Source, a US DOE Office of Science user facility operated for the DOE Office of Science by Argonne National Laboratory under contract number DE-AC02-06CH11357. The NMR experimental work reported here made use of the shared facilities of the UCSB MRSEC (NSF DMR 1720256), a member of the Material Research Facilities Network. The TEM work is supported by the Assistant Secretary for Energy Efficiency and Renewable Energy, Vehicle Technologies Office of the US DOE under contract number DE-LC-000L053 under the programme of Next Generation Cathode. Part of the work was conducted at the William R. Wiley Environmental Molecular Sciences Laboratory, a national scientific user facility sponsored by DOE's Office of Biological and Environmental Research and located at Pacific Northwest National Laboratory (PNNL). PNNL is operated by Battelle for the DOE under contract DE-AC05-76RL01830.

Author contributions

Z.C. planned the project with G.C., Z.L. and B.O.; Z.C. designed, synthesized, characterized and electrochemically tested the proposed compounds with help from Z.L., H.J., H.-M.H., J.H. and Y.C.; B.O. performed DFT calculations and analysed the data; T.C. performed NEB calculations and analysed the data; R.G., V.W. and Z.L. acquired and analysed the NMR data with input from R.J.C.; K.P.K. and L.L. acquired and analysed the STEM data with input from C.W.; Y.S. acquired and analysed SEM data; Y.H. acquired and analysed the mRIXS data with input from W.Y.; and Z.C. acquired and analysed the XAS data. The manuscript was written by Z.C. and was revised by Z.L., B.O., T.C., K.P.K., C.W., R.J.C. and G.C. with help from the other authors. All authors contributed to discussions.

Competing interests

The authors declare no competing interests.

Additional information

Supplementary information The online version contains supplementary material available at <https://doi.org/10.1038/s41560-023-01375-9>.

Correspondence and requests for materials should be addressed to Zhengyan Lun or Gerbrand Ceder.

Peer review information *Nature Energy* thanks Maria Diaz Lopez, Valerie Pralong and the other, anonymous, reviewer(s) for their contribution to the peer review of this work.

Reprints and permissions information is available at www.nature.com/reprints.

Publisher's note Springer Nature remains neutral with regard to jurisdictional claims in published maps and institutional affiliations.

Open Access This article is licensed under a Creative Commons Attribution 4.0 International License, which permits use, sharing, adaptation, distribution and reproduction in any medium or format, as long as you give appropriate credit to the original author(s) and the source, provide a link to the Creative Commons license, and indicate if changes were made. The images or other third party material in this article are included in the article's Creative Commons license, unless indicated otherwise in a credit line to the material. If material is not included in the article's Creative Commons license and your intended use is not permitted by statutory regulation or exceeds the permitted use, you will need to obtain permission directly from the copyright holder. To view a copy of this license, visit <http://creativecommons.org/licenses/by/4.0/>.

© The Author(s) 2023